

Spin Fluctuations in the Rare-Earth Doped Bilayer Nickelates

Honglin Zhou,^{1, 2, *} Xinman Ye,^{3, *} Gang Wang,^{1, 2, *} Devashibhai Adroja,^{4, 5, *} David Tam,⁶ Michael Marek Koza,⁶ Zhilun Lu,⁷ Jinguang Cheng,^{1, 2, †} Dao-Xin Yao,^{3, ‡} and Huiqian Luo^{1, §}

¹Beijing National Laboratory for Condensed Matter Physics,

Institute of Physics, Chinese Academy of Sciences, Beijing 100190, China

²School of Physical Sciences, University of Chinese Academy of Sciences, Beijing 100190, China

³Institute of Neutron Science and Technology, Guangdong Provincial Key Laboratory of Magnetoelectric Physics and Devices, School of Physics, Sun Yat-Sen University, Guangzhou 510275, China

⁴ISIS Neutron and Muon Source, Rutherford Appleton Laboratory, Chilton, Didcot OX11 0QX, United Kingdom

⁵Physics Department, University of Johannesburg, Auckland Park 2006, South Africa

⁶Institut Laue-Langevin, 71 Avenue des Martyrs, 38000 Grenoble, France

⁷School of Chemical and Process Engineering, University of Leeds, Leeds, West Yorkshire LS2 9JT, UK

(Dated: January 22, 2026)

Spin fluctuations have been generally believed as the pairing glue of high- T_c superconductivity. Recent inelastic neutron scattering (INS) studies have revealed a weak flat spin-fluctuation signal around 45 meV in the bilayer nickelate $\text{La}_3\text{Ni}_2\text{O}_{7-\delta}$, suggesting strong interlayer and weak intralayer magnetic couplings ($SJ_{\perp} \approx 60$ meV, $SJ_{\parallel} \leq 3.5$ meV) in contrast to cuprate and pnictide superconductors. Here, we report further INS studies on the Pr and Nd doped $\text{La}_3\text{Ni}_2\text{O}_{7-\delta}$ powder samples at ambient pressure. Besides the crystalline electric field excitations at low energies, we have found that the 45 meV flat mode splits into two modes in doped compounds, along with another weak mode at about 60 meV, where the spin fluctuations in $\text{La}_2\text{NdNi}_2\text{O}_{7-\delta}$ are stronger than $\text{La}_3\text{Ni}_2\text{O}_{7-\delta}$ and $\text{La}_2\text{PrNi}_2\text{O}_{7-\delta}$. Based on an effective Heisenberg model by only considering the nearest-neighbor exchange couplings on the stripe-type antiferromagnetic orders, we conclude that the interlayer coupling SJ_{\perp} is enhanced to about 69 meV and 73 meV for Pr and Nd doped samples, respectively. Our results highlight the crucial role of interlayer coupling in the rare-earth doped bilayer nickelates, which towards to promote high T_c via interlayer $s\pm$ pairing.

I. INTRODUCTION

Spin fluctuations are arguably the common thread in understanding the pairing mechanism of high- T_c superconductivity^{1–11}. In cuprates, while the spin waves emerge at the Néel-type antiferromagnetic (AF) wavevector (\mathbf{Q}_{AF}) in the parent compound and persist to high energy over than 200 meV^{2,4}, the low-energy spin fluctuations form a collective spin resonance mode in the superconducting state of doped compounds¹². The intensity of resonance mode behaves like a superconducting order parameter with a peak energy (E_R) linearly scaling with T_c and a downward dispersion confined by the d -wave superconducting gap¹³. Similar scenario is established in the iron-based superconductors, where both strong spin fluctuations and spin resonance have been extensively discovered around the stripe-type wavevector of iron pnictides^{4–8}, and the resonance dispersion turns to depend on the fermiology in the multi-band $s\pm$ -wave pairing picture^{14–19}. Notably, the spin wave dispersion in the AF ordered parent compounds can be described by an effective Heisenberg model with dominated in-plane exchange couplings (J_{1a}, J_{1b}, J_2) and a weak out-of-plane coupling (J_c)^{4,5}. The spin fluctuations keep such memory in the superconducting compounds but become quasi-two-dimensional (quasi-2D) like with nearly zero J_c ^{5–7}. Both the high energy scale determined by the in-plane exchange couplings of local moments and the strong coupling with itinerant electrons in the spin fluctuations are essential to understand the high- T_c mechanism^{19–21}.

The bilayer nickelates $\text{La}_{3-x}R_x\text{Ni}_2\text{O}_{7-\delta}$ ($R = \text{Pr}, \text{Nd}, \text{Sm}, \dots$) recently catalogued as a new family of high- T_c superconductors^{22–29}, provide a distinct vision of high- T_c mechanism related to spin fluctuations^{30–43}. The $\text{La}_3\text{Ni}_2\text{O}_7$ compound, referred as the bilayer Ruddlesden-Popper phase, crystallizes in an orthorhombic *Amam* structure with alternating stacks of two NiO_2 planes and tilted octahedra³⁰. The nominal valence state is $\text{Ni}^{2.5+}$ for $3d^{7.5}$ electronic configuration with half-filled d_{z^2} and quarter-filled $d_{x^2-y^2}$ orbitals near the Fermi level^{37–43}. With increasing pressure, the bond angle of Ni-O-Ni along c axis changes from 168° to 180° , leading to an orthorhombic *Fmmm* or tetragonal *I4/mmm* phase showing a high- T_c superconductivity up to 80 K^{22,43}. Although the microscopic mechanism remains inconclusive, the interlayer coupling is generally believed as a crucial key responsible for the superconducting pairing^{40–42}. Possible magnetic orders are also proposed by neutron diffraction, positive muon spin relaxation ($\mu^+\text{SR}$) and nuclear magnetic resonance (NMR) measurements^{44–52}. Indeed, the physical pressure probably drives the emergence of a hole pocket of d_{z^2} orbital, or uniformly enhances the bandwidth, in either case it will yield a predominant $s\pm$ -wave pairing triggered by spin fluctuations^{53–67}. The rare earth doping provides additional chemical pressure to modify the interlayer coupling and the d_{z^2} orbital electronic structure^{68–75}, which could potentially enhance T_c as demonstrated in $\text{La}_2\text{SmNi}_2\text{O}_{7-\delta}$ and $\text{La}_{0.6}\text{Nd}_{2.4}\text{Ni}_2\text{O}_{7-\delta}$ ^{76–80}.

Here we report an inelastic neutron scattering (INS)

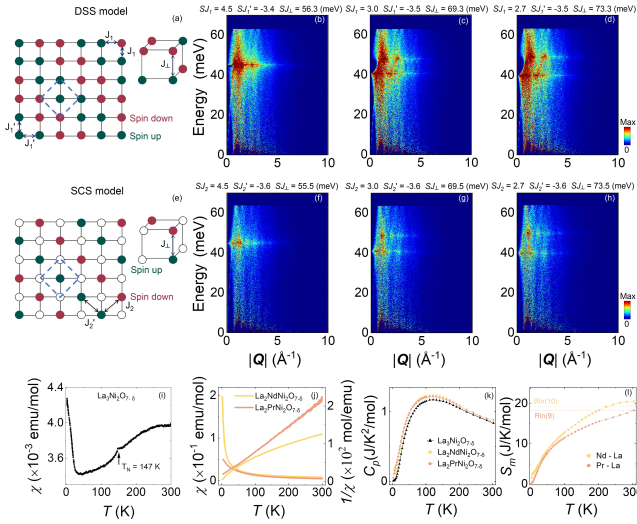


FIG. 1: (a)-(h) SpinW calculations based on the double spin stripe (DSS) and the single spin-charge stripe (SCS) AF orders using different combinations of exchange couplings. The nearest-neighbor intralayer exchange couplings J_1, J'_1 in DSS model (or J_2, J'_2 in SCS model) and interlayer exchange coupling J_{\perp} are indicated in (a) and (e). The green, red and white balls represent the spin up, spin down and nonmagnetic Ni atoms, respectively⁸². (i) Magnetic susceptibility χ of $\text{La}_3\text{Ni}_2\text{O}_{7-\delta}$. The anomaly at $T_N = 147$ K probably responses to the AF transition. (j) χ and its inverse $1/\chi$ of $\text{La}_2\text{NdNi}_2\text{O}_{7-\delta}$ and $\text{La}_2\text{PrNi}_2\text{O}_{7-\delta}$. The dashed straight lines are Curie-Weiss fittings below 50 K. (k) Heat capacity C_p versus T for three compounds. (l) Magnetic entropy of Pr and Nd doped samples from the integration of C_m/T . Here C_m is obtained by subtracting the C_p of $\text{La}_3\text{Ni}_2\text{O}_{7-\delta}$.

study on the Nd and Pr doped bilayer nickelates $\text{La}_2\text{PrNi}_2\text{O}_{7-\delta}$ and $\text{La}_2\text{NdNi}_2\text{O}_{7-\delta}$ powder samples at ambient pressure. Previous INS on $\text{La}_3\text{Ni}_2\text{O}_{7-\delta}$ powder sample has revealed a weak flat spin-fluctuation signal around 45 meV, which could be interpreted as a result of strong interlayer ($SJ_{\perp} \approx 60$ meV) and weak intralayer ($SJ_{\parallel} \leq 3.5$ meV) magnetic couplings for stripe-type AF orders⁸¹. Such conclusion is confirmed by the measurements of resonant inelastic X-ray scattering (RIXS) and INS on single-crystalline samples^{82,83}. In Pr and Nd doped samples, we have found that the SJ_{\perp} is further enhanced to about 70 meV. The main feature is two splitting flat modes of spin fluctuations around 45 meV, which can be theoretically simulated based on the stripe-type AF orders by only considering the nearest-neighbor exchange couplings (Fig. 1(a)-(h)). Such enhancement of J_{\perp} possibly accounts for the increased T_c from 80 K to near 100 K in rare-earth doped $\text{La}_3\text{Ni}_2\text{O}_{7-\delta}$ ^{77,80}.

II. RESULTS AND DISCUSSION

A. Sample characterization

Powder sample of $\text{La}_2\text{LnNi}_2\text{O}_{7-\delta}$ ($\text{Ln}=\text{La, Pr, Nd}$) are prepared by the sol-gel method^{26,70,84,85}. The magnetic susceptibility χ and heat capacity C_p results are presented in Fig. 1 (i)-(l). While a weak anomaly of χ is found at 147 K for pure La sample, probably related to the stripe-type AF phase transition⁴⁴⁻⁴⁸. The χ of Nd samples show a Curie-Weiss (CW) behavior as indicating by the linear $1/\chi$ vs T (Fig. 1(i)(j)), CW-fitting of χ below 50 K gives the effective magnetic moments $\mu_{\text{eff}}(\text{Nd})=2.8 \mu_{\text{B}}$ and $\mu_{\text{eff}}(\text{Pr})=3.7 \mu_{\text{B}}$, consistent with the 4f electron contributions. No clear phase transition can be identified in C_p except a very broad hump around 100 K. Overall, all three samples have similar temperature dependence of C_p , suggesting almost the same contribution from phonons. Thus the magnetic heat capacity C_m (or 4f-contribution C_{4f}) can be deduced by deducting C_p of La sample, and the magnetic entropy S_m can be obtained by integrating C_m/T . The crystalline electric field (CEF) contribution from Pr^{3+} ($4f^2, J=4$) and Nd^{3+} ($4f^3, J=9/2$) atoms is expected to yield a plateau at $R\ln(9)=17.7 \text{ J mol}^{-1}\text{K}^{-1}$ and $R\ln(10)=19.1 \text{ J mol}^{-1}\text{K}^{-1}$, respectively⁸⁶. However, this is not the case in Fig. 1(l), where $S_m(\text{Nd-La})$ exceeds the plateau value, suggesting additional contribution from spin fluctuations. It should be noticed that the absence of anomaly in χ and C_p of Pr and Nd doped samples cannot rule out the possibility of a weak magnetic order of Ni. In fact, μ^+ SR measurements have estimated $m_{\text{Ni}} \approx 0.22/0.42 \mu_{\text{B}}$ when the magnetic moments align along c/ab axis for pure La sample⁴⁸, and the neutron powder diffraction give $m_{\text{Ni}} \approx 0.15/0.85 \mu_{\text{B}}$ on low and high-moment sites of $\text{La}_2\text{PrNi}_2\text{O}_7$ ⁴⁶. However, it is clear that the rare-earth ions do not form any long-range magnetic order at low temperature in nickelates.

B. Inelastic neutron scattering

To search the spin excitations of $\text{La}_2\text{NdNi}_2\text{O}_{7-\delta}$, we have performed INS measurements at the time-of-flight spectrometer MERLIN, ISIS Neutron and Muon Source of UK^{87,88}. We summarize the raw data in Fig. 2(a)-(h) by plotting the 2D slice of energy versus the absolute momentum transfer $|\mathbf{Q}|$ (referred as Q in the following) for different incident neutron energies $E_i = 15, 24, 50$ and 79 meV measured at $T = 5$ and 110 K. Clear Q -independent CEF excitations are observed at the energy transfer $E = 5.5$ and 22 meV, which feature as peaks in 1D E -cuts (Fig. 2(i)-(k)) with stronger intensity at 5 K. Although the data set of $E_i = 79$ meV is contaminated by strong phonon scattering from the sample and aluminum can at high Q region, the difference between 5 K and 110 K 1D E -cut shows three new peak features at $E = 43, 48$ and 60 meV, which cannot be described by

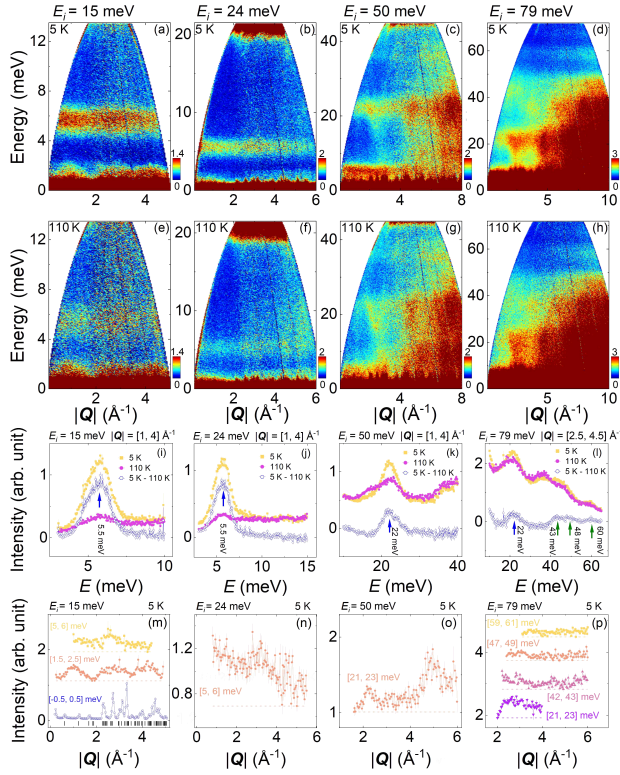


FIG. 2: INS spectra of $\text{La}_2\text{NdNi}_2\text{O}_{7-\delta}$ collected at MERLIN. (a)-(d) Data measured at 5 K with incident energy $E_i = 15, 24, 50$ and 79 meV. (e)-(h) Data measured at 110 K with similar E_i s. (i)-(l) E -cuts at $T = 5$ K, 110 K, and their differences with Bose corrections⁸⁵. The blue arrows mark the CEF excitations, and the green arrows mark the possible spin excitations. (m)-(p) Q -cuts at $T = 5$ K at the typical energy windows of excitations. The data is vertically shifted for clarity. The elastic cut with $E = [-0.5, 0.5]$ meV is also presented in (m), where all nuclear peaks are marked by vertical bars.

CEF excitations of Nd^{3+} , and are possible spin excitations (Fig. 2(l))⁸¹⁻⁸³. To confirm the magnetic origin of these features, we then integrate the intensity at 5 K focusing on these specific energy windows and plot the 1D Q -cuts in Fig. 2(m)-(p). Most of them show a decreasing intensity by increasing Q , a typical evidence for magnetic scattering. The abrupt increase of the 1D cut $E = [21, 23]$ meV in Fig. 2(o) is due to phonon backgrounds at high Q . The positions of Bragg peaks can be found in the quasi-elastic cut with $E = [-0.5, 0.5]$ meV for $E_i = 15$ meV measurement (Fig. 2(m)). No clear magnetic peaks could be identified, and most nuclear peaks locate above 2 \AA^{-1} . Thus the broad peak of the intensity with $E = [1.5, 2.5]$ meV from $Q = 0.5$ to 2 \AA^{-1} could be also spin excitations emerging from low energy, since only two tiny nuclear peaks exist in this small Q region⁸¹. No signals related to any spin excitations above 70 meV are observed in the $E_i = 160$ meV data, which is consistent with the RIXS and INS results on single crystals^{82,83}.

Further INS measurements on three samples $\text{La}_2\text{LnNi}_2\text{O}_{7-\delta}$ ($\text{Ln} = \text{La}, \text{Pr}, \text{Nd}$) were carried out

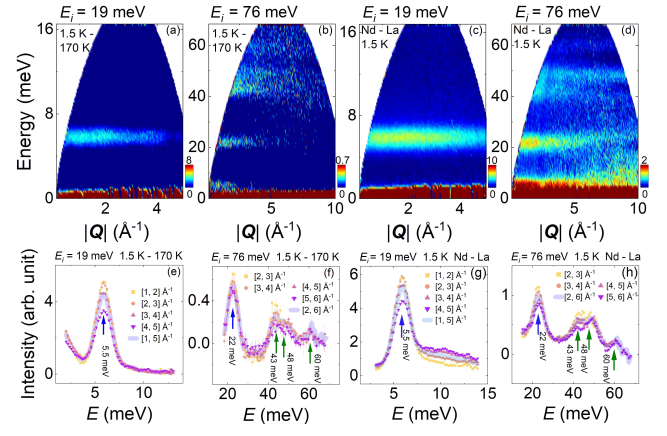


FIG. 3: INS spectra of $\text{La}_2\text{NdNi}_2\text{O}_{7-\delta}$ collected at PANTHER with $E_i = 19$ and 76 meV. (a) and (b) Spectra after subtracting 170 K from 1.5 K data. (c) and (d) Spectra after subtracting $\text{La}_3\text{Ni}_2\text{O}_{7-\delta}$ from $\text{La}_2\text{NdNi}_2\text{O}_{7-\delta}$ data at $T = 1.5$ K. (e)-(h) E -cuts at different Q regions corresponding to (a)-(d). Bose corrections are applied to (e) and (f)⁸⁵. The blue arrows mark the CEF excitations at 5.5 and 22 meV, and the green arrows mark the spin excitations at 43, 48 and 60 meV.

at the time-of-flight spectrometer PANTHER with incident neutron energy $E_i = 12.5, 19$ and 76 meV^{85,89,90}. Fig. 3 presents the results of $\text{La}_2\text{NdNi}_2\text{O}_{7-\delta}$ collected at PANTHER. Again, the energy levels of CEF excitations can be easily observed at $E = 5.5$ and 22 meV from the 1D E -cut by subtracting the 170 K data from 1.5 K data (Fig. 3(a), (b), (e) and (f)). The spin excitations at high energy are even more clearly to see the splitting signals at $E = 43$ and 48 meV closed to the case of flat 45 meV mode in $\text{La}_3\text{Ni}_2\text{O}_{7-\delta}$. Another feature at $E = 60$ meV is also observed (Fig. 3(b) and (f)). To double check the magnetic nature of these signals, we then take the data set of $\text{La}_3\text{Ni}_2\text{O}_{7-\delta}$ measured at the same condition as the reference of phonon background, since the 45 meV signal in the undoped sample is much weaker than the Nd-doped sample, but the phonon contribution at high Q is similar. The subtraction of Nd - La data set gives promising results for all above mentioned energy levels, especially for two splitting modes around 45 meV. It seems that the splitting of spin excitations around 45 meV develops upon increasing Q , which is an unique feature of the bilayer nickelates⁸¹, and has never been observed in cuprate or pnictide superconductors¹⁻⁵.

After establishing the excitations in $\text{La}_2\text{NdNi}_2\text{O}_{7-\delta}$, we then present the INS results of $\text{La}_2\text{PrNi}_2\text{O}_{7-\delta}$ by processing similar analyses (Fig. 4). Given that Pr^{3+} is a non-Kramers ion with multiplet state⁸⁶, the CEF excitations are populated in 4 doublet levels with broad distributions at high temperature. Possible energy levels could be identified at $E = 2, 3.5, 4.2$ and 6 meV from the 1.5 K and subtracted data (Fig. 4(a),(b),(e) and (f)). No magnetic peaks could be identified in the elastic Q -cut, and the CEF excitations decrease with increasing Q (Fig. 4(i) and (j)). The splitting of spin excitations around 45

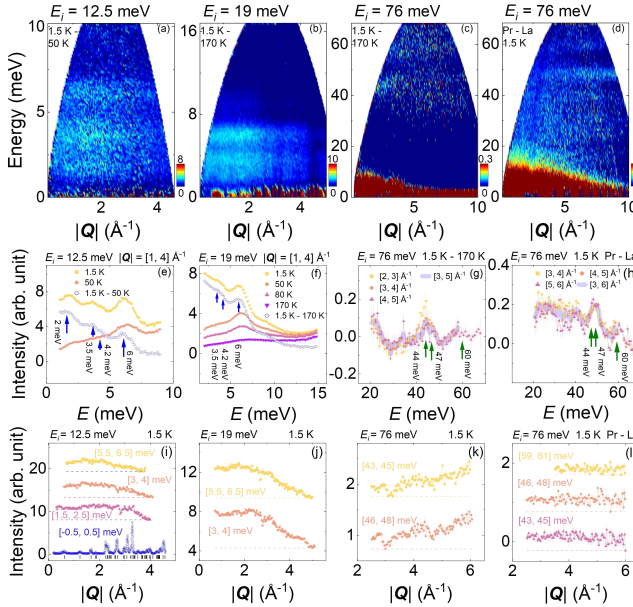


FIG. 4: INS spectra of $\text{La}_2\text{PrNi}_2\text{O}_{7-\delta}$ collected at PANTHER with $E_i = 12.5, 19$ and 76 meV. (a) Spectrum of subtracting 50 K from 1.5 K data ($E_i = 12.5$ meV). (b)-(c) Spectra after subtracting 170 K from 1.5 K data ($E_i = 19$ and 76 meV). (d) Spectra for $E_i = 76$ meV after subtracting $\text{La}_3\text{Ni}_2\text{O}_{7-\delta}$ data at $T = 1.5$ K. (e)-(h) E -cuts at different regions corresponding to (a)-(d). Bose corrections are applied to panel (e), (f) and (g)⁸⁵. The blue arrows mark the CEF excitations at $2, 3.5$ and 6 meV, and the green arrows mark the spin excitations at $44, 47$ meV and 60 meV. (i)-(l) Q -cuts at $T = 1.5$ K by focusing energy windows. The elastic cut with $E = [-0.5, 0.5]$ is also presented in panel (i), where all nuclear peaks are marked by vertical bars.

meV still exists, but becomes weak at about $E = 44$ and 47 meV, along with weaker signals at $E = 60$ meV (Fig. 4(c), (d), (g) and (h)). It is hard to distinguish the Q -dependence of magnetic and phonon scatterings by doing similar subtraction (Fig. 4(k) and (l))⁸⁵. Further measurements on single crystals are highly desired.

C. Theoretical analyses

Finally, we discuss the INS results using four theoretical models: single spin-charge stripe order (SCS), double spin stripe order (DSS), A-type AF order (AFM-A), and G-type AF order (AFM-G). We have performed numerical calculations of spin excitation spectra based on the linear spin wave theory and the SpinW software package⁸⁵. According to previous reports, the stripe-type AF orders SCS and DSS are the most likely cases in the bilayer nickelates: where Ni^{2+} spin and Ni^{3+} charge stripes diagonally intertwine in SCS (Fig. 1(e)), or doubly ordered without charge inhomogeneity in DSS (Fig. 1(a)), both of them have the same wavevector $\mathbf{Q}_{\text{AF}} = (0.25, 0.25)$ in the quasi-tetragonal lattice^{46,82}. Therefore, by considering the nearest-neighbor interlayer and

intralayer interactions, we can construct a simple Heisenberg Hamiltonian:

$$H = J_\alpha \sum_{\langle i,j \rangle} S_i \cdot S_j + J'_\alpha \sum_{\langle i,j \rangle'} S_i \cdot S_j + J_\perp \sum_i S_i^t \cdot S_i^b, \quad (1)$$

where J_α and J'_α are the AF and ferromagnetic (FM) intralayer nearest-neighbor interactions, respectively. We use $\alpha = 1, 2$ to denote the case of DSS and SCS models for their different bonding lengths (3.8 Å and 5.4 Å). J_\perp is the interlayer nearest-neighbor interaction at the same site with top and bottom layer spins (S^t, S^b), where the effective spin S arises from the total spin contributions of different orbitals. Since the in-plane lattice is not exactly tetragonal, it is reasonable to have different absolute value of J_α and J'_α . For the stripe-type models, we adopted the parameters shown in Table I to describe the INS data of all three samples, the obtained spectra are presented in Fig. 1(b)-(d) and (f)-(h). Based on the simulation results of the DSS and SCS models, it can be clearly observed that the interlayer interaction (SJ_\perp) is much stronger than the intralayer interaction (SJ_α, SJ'_α). In the doped case, SJ_\perp increases significantly, while the intralayer interaction undergo changes, resulting in a band gap between the acoustic and optical branches in DSS model, or anisotropic in-plane bandtop in SCS model⁸⁵. It finally turns to the occurrence of splitting flat modes around 45 meV in our powder INS measurements. Such phenomenon is more pronounced in $\text{La}_2\text{NdNi}_2\text{O}_{7-\delta}$ due to its larger J_\perp . On the other hand, the AFM-A and AFM-G models with isotropic intralayer interactions cannot produce the splitting flat-band like spectrum but only wave-like characteristics⁸⁵, thus they can be ruled out in the bilayer nickelate system.

TABLE I: Model parameters for DSS (top) and SCS (bottom)

Couplings	$\text{La}_3\text{Ni}_2\text{O}_{7-\delta}$	$\text{La}_2\text{PrNi}_2\text{O}_{7-\delta}$	$\text{La}_2\text{NdNi}_2\text{O}_{7-\delta}$
SJ_1 (meV)	4.5	3.0	2.7
SJ'_1 (meV)	-3.4	-3.5	-3.5
SJ_\perp (meV)	56.3	69.3	73.3
SJ_2 (meV)	4.5	3.0	2.7
SJ'_2 (meV)	-3.6	-3.6	-3.6
SJ_\perp (meV)	55.5	69.5	73.5

The variation in spin couplings may originate from the doping effect on the electronic properties of $\text{La}_3\text{Ni}_2\text{O}_{7-\delta}$, which introduces chemical pressure to change the orbital correlations⁶⁸⁻⁷⁵. The ionic radii of Pr and Nd are smaller than that of La, yielding a chemical pressure to compress the lattice by reducing the interlayer spacing and Ni-O-Ni bond angles⁸⁵. Such effect probably enhances the overlap between $\text{Ni}-d_{z^2}$ and $\text{O}-p_z$ orbitals, but improves the critical pressure of superconductivity⁷⁶⁻⁸⁰. The antibonding state of the d_{z^2} orbital shifts toward higher energy, which further strengthens the interlayer coupling. Meanwhile, the in-plane Ni-O bond length

changes moderately, exerting little influence on the in-plane orbital overlap. Therefore, the orbital-dependent effect from rare-earth doping is mainly concentrated on the d_{z^2} orbital, giving a negligible impact on the electronic structure of the intralayer $d_{x^2-y^2}$ orbital. As a result, the orbital density and energy level distribution remain basically stable, and the intralayer coupling is almost unchanged overall. Since the ionic radius of Pr is slightly larger than that of Nd, the influence of the aforementioned effects is relatively weaker, and the corresponding variation is less pronounced, which is indeed consistent with our experimental data. If the interlayer $s\pm$ -pairing indeed dominates under pressure, assuming $SJ_{\perp} \propto T_c^{33-36}$, $SJ_{\perp} = 73$ meV would expect a promotion of T_c to about 104 K in $\text{La}_2\text{NdNi}_2\text{O}_{7-\delta}$, surprisingly consistent with recent reports⁷⁶⁻⁸⁰.

III. CONCLUSIONS

We have identified the spin excitations in the rare-earth doped bilayer nickelates $\text{La}_2\text{NdNi}_2\text{O}_{7-\delta}$ and $\text{La}_2\text{PrNi}_2\text{O}_{7-\delta}$. The flat feature of spin spectrum in $\text{La}_3\text{Ni}_2\text{O}_{7-\delta}$ keeps in Nd and Pr doped compounds, but

it splits into two flat modes around 45 meV. By analyzing the spin excitations with an effective Heisenberg model with only the nearest-neighbor exchange couplings, we reveal that the interlayer coupling J_{\perp} is significantly enhanced in Nd and Pr doped samples. The stronger spin excitations and larger J_{\perp} in $\text{La}_2\text{NdNi}_2\text{O}_{7-\delta}$ probably support higher T_c under pressure than the parent compound $\text{La}_3\text{Ni}_2\text{O}_{7-\delta}$. Our results enlighten the mechanism investigations on the magnetically driven high- T_c superconductivity in nickelates.

This work is supported by the National Key Research and Development Program of China (Grants No. 2023YFA1406100, No. 2022YFA1403800 and No. 2025YFE0202100) and the National Natural Science Foundation of China (Grants No. 12574165, No. 12274444, and No. 12025408). DTA thank EPSRC-UK (Grant No. EP/W00562X/1) and the CAS for PIFI fellowship. Measurements on MERLIN were supported by the beam time allocation (Express proposals: 2590110 and 2590111) from the Science and Technology Facilities Council. Collected data from PANTHER (Proposal 4-04-536) are available at DOI:10.5291/ILL-DATA.4-04-536.

* These authors made equal contributions to this paper

† jgcheng@iphy.ac.cn

‡ yaodaox@mail.sysu.edu.cn

§ hqluo@iphy.ac.cn

- ¹ D. J. Scalapino, A common thread: the pairing interaction for unconventional superconductors. *Rev. Mod. Phys.* **84**, 1383 (2012).
- ² J. M. Tranquada, G. Xu, and I. A. Zaliznyak, Superconductivity, antiferromagnetism, and neutron scattering. *J. Magn. Magn. Mater.* **350**, 148 (2014).
- ³ B. D. White, J. D. Thompson, and M. B. Maple, Unconventional superconductivity in heavy-fermion compounds. *Physica C: Superconductivity* **514**, 246 (2015).
- ⁴ P. Dai, J. Hu, and E. Dagotto, Magnetism and its microscopic origin in iron-based high-temperature superconductors. *Nat. Phys.* **8**, 709 (2012).
- ⁵ P. Dai, Antiferromagnetic order and spin dynamics in iron-based superconductors. *Rev. Mod. Phys.* **87**, 855 (2015).
- ⁶ D. C. Johnston, The puzzle of high temperature superconductivity in layered iron pnictides and chalcogenides. *Adv. Phys.* **59**, 803 (2010).
- ⁷ X. Chen, P. Dai, D. Feng, T. Xiang, and F.-C. Zhang, Iron-based high transition temperature superconductors. *Natl. Sci. Rev.* **1**, 371 (2014).
- ⁸ A. D. Christianson, E. A. Goremychkin, R. Osborn, *et al.* Unconventional superconductivity in $\text{Ba}_{0.6}\text{K}_{0.4}\text{Fe}_2\text{As}_2$ from inelastic neutron scattering. *Nature* **456**, 930 (2008).
- ⁹ Q. Gu and H.-H. Wen, Superconductivity in nickel-based 112 systems. *The Innovation* **3**, 100202 (2022).
- ¹⁰ Y. Wang, K. Jiang, J. Ying, T. Wu, J. Cheng, J. Hu, and X. Chen, Recent progress in nickelate superconductors. *Natl. Sci. Rev.* **12**, nwaf373 (2025).
- ¹¹ Z. Wang, H.-J. Zhang, K. Jiang, and F.-C. Zhang,

Self-doped molecular Mott insulator for bilayer high-temperature superconducting $\text{La}_3\text{Ni}_2\text{O}_7$. *Natl. Sci. Rev.* **12**, nwaf353 (2025).

- ¹² M. Eschrig, The effect of collective spin-1 excitations on electronic spectra in high- T_c superconductors. *Adv. Phys.* **55**, 47 (2006).
- ¹³ Y. Sidis, S. Pailhès, V. Hinkov, B. Fauqué, C. Ulrich, L. Capogna, *et al.* Inelastic neutron scattering study of spin excitations in the superconducting state of high temperature superconductors. *C. R. Phys.* **8**, 745 (2007).
- ¹⁴ R. Zhang, W. Wang, T. A. Maier, M. Wang, M. B. Stone, S. Chi, *et al.*, Neutron spin resonance as a probe of Fermi surface nesting and superconducting gap symmetry in $\text{Ba}_{0.67}\text{K}_{0.33}(\text{Fe}_{1-x}\text{Co}_x)_2\text{As}_2$, *Phys. Rev. B* **98**, 060502(R) (2018).
- ¹⁵ T. Xie, C. Liu, T. Fennell, U. Stuhr, S. Li, and H. Luo, Dispersion of neutron spin resonance mode in $\text{Ba}_{0.67}\text{K}_{0.33}\text{Fe}_2\text{As}_2$. *Chin. Phys. B* **30**, 127402 (2021).
- ¹⁶ W. Hong, L. Song, B. Liu, Z. Li, Z. Zeng, Y. Li, *et al.* Neutron spin resonance in a quasi-two-dimensional iron-based superconductor. *Phys. Rev. Lett.* **125**, 117002 (2020).
- ¹⁷ W. Hong, H. Zhou, Z. Li, Y. Li, U. Stuhr, A. Pokhriyal, *et al.* Interlayer coupling in the superconducting state of iron-based superconductors. *Phys. Rev. B* **107**, 224514 (2023).
- ¹⁸ Y. Li, D. Wu, Y. Shu, B. Liu, U. Stuhr, G. Deng, *et al.* Neutron spin resonance near a Lifshitz transition in overdoped $\text{Ba}_{0.4}\text{K}_{0.6}\text{Fe}_2\text{As}_2$. *Chin. Phys. Lett.* **42**, 067405 (2025).
- ¹⁹ Z. Li, W. Hong, T. Xie, C. Liu, and H. Luo, Spin excitation spectra of iron pnictide superconductors. *Acta Phys. Sin.* **74**, 017401 (2025).
- ²⁰ F. Wang and D. H. Lee, The electron-pairing mechanism of iron-based superconductors, *Science* **332**, 200 (2011).
- ²¹ M. Wang, C. Zhang, X. Lu, G. Tan, H. Luo, Y. Song, *et al.*

Doping dependence of spin excitations and its correlations with high-temperature superconductivity in iron pnictides, *Nat. Commun.* **4**, 2874 (2013).

²² H. Sun, M. Huo, X. Hu, J. Li, Z. Liu, Y. Han, *et al.* Signatures of superconductivity near 80 K in a nickelate under high pressure. *Nature* **621**, 493 (2023).

²³ Y. Zhang, D. Su, Y. Huang, Z. Shan, H. Sun, M. Huo, *et al.* High-temperature superconductivity with zero resistance and strange-metal behaviour in $\text{La}_3\text{Ni}_2\text{O}_{7-\delta}$, *Nat. Phys.* **20**, 1269 (2024).

²⁴ N. Wang, G. Wang, X. Shen, J. Hou, J. Luo, X. Ma, *et al.* Bulk high-temperature superconductivity in pressurized tetragonal $\text{La}_2\text{PrNi}_2\text{O}_{7-\delta}$. *Nature* **634**, 579 (2024).

²⁵ J. Hou, P.-T. Yang, Z.-Y. Liu, J.-Y. Li, P.-F. Shan, L. Ma, *et al.* Emergence of high-temperature superconducting phase in pressurized $\text{La}_3\text{Ni}_2\text{O}_7$ crystals. *Chin. Phys. Lett.* **40**, 117302 (2023).

²⁶ G. Wang, N. N. Wang, X. L. Shen, J. Hou, L. Ma, L. F. Shi, *et al.* Pressure-induced superconductivity in polycrystalline $\text{La}_3\text{Ni}_2\text{O}_{7-\delta}$. *Phys. Rev. X* **14**, 011040 (2024).

²⁷ E. K. Ko, Y. Yu, Y. Liu, L. Bhatt, J. Li, V. Thampy, *et al.* Signatures of ambient pressure superconductivity in thin film $\text{La}_3\text{Ni}_2\text{O}_7$. *Nature* **638**, 935 (2025).

²⁸ G. Zhou, W. Lv, H. Wang, Z. Nie, Y. Chen, Y. Li, *et al.* Ambient-pressure superconductivity onset above 40 K in $(\text{La},\text{Pr})_3\text{Ni}_2\text{O}_7$ films. *Nature* **640**, 641 (2025).

²⁹ W. Wu, Z. Luo, D. X. Yao, and M. Wang, Superexchange and charge transfer in the nickelate superconductor $\text{La}_3\text{Ni}_2\text{O}_7$ under pressure. *Sci. China-Phys. Mech. Astron.* **67**, 117402 (2024).

³⁰ M. Wang, H. H. Wen, T. Wu, D.-X. Yao, and T. Xiang, Normal and superconducting properties of $\text{La}_3\text{Ni}_2\text{O}_7$. *Chin. Phys. Lett.* **41**, 077402 (2024).

³¹ Z. Liu, M. Huo, J. Li, Q. Li, Y. Liu, Y. Dai, *et al.* Electronic correlations and partial gap in the bilayer nickelate $\text{La}_3\text{Ni}_2\text{O}_7$, *Nat. Commun.* **15**, 7570 (2024).

³² Z. Liao, L. Chen, G. Duan, Y. Wang, C. Liu, R. Yu, and Q. Si, Electron correlations and superconductivity in $\text{La}_3\text{Ni}_2\text{O}_7$ under pressure tuning. *Phys. Rev. B* **108**, 214522 (2023).

³³ Y.-f. Yang, G.-M. Zhang, and F.-C. Zhang, Interlayer valence bonds and two-component theory for high- T_c superconductivity of $\text{La}_3\text{Ni}_2\text{O}_7$ under pressure, *Phys. Rev. B* **108**, L201108 (2023).

³⁴ Q. Qin and Y.-f. Yang, High- T_c superconductivity by mobilizing local spin singlets and possible route to higher T_c in pressurized $\text{La}_3\text{Ni}_2\text{O}_7$, *Phys. Rev. B* **108**, L140504 (2023).

³⁵ Q. Qin, J. Wang, and Y.-f. Yang, Frustrated superconductivity and intrinsic reduction of T_c in trilayer nickelate, *The Innovation Materials* **2**, 100102 (2024).

³⁶ X.-Z. Qu, D.-W. Qu, J. Chen, C. Wu, F. Yang, W. Li, and G. Su, Bilayer $t-J-J_\perp$ model and magnetically mediated pairing in the pressurized nickelate $\text{La}_3\text{Ni}_2\text{O}_7$. *Phys. Rev. Lett.* **132**, 036502 (2024).

³⁷ J. J. Yang, D.-X. Yao, and H. Q. Wu, Correlation effects in a simplified bilayer two-orbital Hubbard model at half filling. *Phys. Rev. B* **110**, 235155 (2024).

³⁸ T. Kaneko, H. Sakakibara, M. Ochi, and K. Kuroki, Pair correlations in the two-orbital Hubbard ladder: Implications for superconductivity in the bilayer nickelate $\text{La}_3\text{Ni}_2\text{O}_7$. *Phys. Rev. B* **109**, 045154 (2024).

³⁹ Z. Ouyang, M. Gao, and Z.-Y. Lu, Absence of electron-phonon coupling superconductivity in the bilayer phase of $\text{La}_3\text{Ni}_2\text{O}_7$ under pressure. *npj Quantum Mater.* **9**, 80 (2024).

⁴⁰ S. Ryee, N. Witt, and T. O. Wehling, Quenched pair breaking by interlayer correlations as a key to superconductivity in $\text{La}_3\text{Ni}_2\text{O}_7$. *Phys. Rev. Lett.* **133**, 096002 (2024).

⁴¹ K. Jiang, Z. Wang, and F.-C. Zhang, High-Temperature Superconductivity in $\text{La}_3\text{Ni}_2\text{O}_7$, *Chin. Phys. Lett.* **41**, 017402 (2024).

⁴² C. Lu, Z. Pan, F. Yang, and C. Wu, Interlayer-coupling-driven high-temperature superconductivity in $\text{La}_3\text{Ni}_2\text{O}_7$ under pressure. *Phys. Rev. Lett.* **132**, 146002 (2024).

⁴³ J. Li, D. Peng, P. Ma, H. Zhang, Z. Xing, X. Huang, *et al.* Identification of superconductivity in bilayer nickelate $\text{La}_3\text{Ni}_2\text{O}_7$ under high pressure up to 100 GPa. *Natl. Sci. Rev.* **12**, nwaf220 (2025).

⁴⁴ S. Taniguchi, T. Nishikawa, Y. Yasui, Y. Kobayashi, J. Takeda, S. Shamoto, and M. Sato, Transport, magnetic and thermal properties of $\text{La}_3\text{Ni}_2\text{O}_{7-\delta}$, *J. Phys. Soc. Jpn.* **64**, 1644 (1995).

⁴⁵ Z. Liu, H. Sun, M. Huo, X. Ma, Y. Ji, E. Yi, *et al.* Evidence for charge and spin density waves in single crystals of $\text{La}_3\text{Ni}_2\text{O}_7$ and $\text{La}_3\text{Ni}_2\text{O}_6$, *Sci. China-Phys. Mech. Astron.* **66**, 217411 (2023).

⁴⁶ I. Plokhikh, T. J. Hicken, L. Keller, V. Pomjakushin, S. H. Moody, P. Foury-Leykian, J. J. Krieger, H. Luetkens, Z. Guguchia, R. Khasanov, and D. J. Gawryluk, Unraveling spin density wave order in layered nickelates $\text{La}_3\text{Ni}_2\text{O}_7$ and $\text{La}_2\text{PrNi}_2\text{O}_7$ via Neutron Diffraction. arXiv:2503.05287.

⁴⁷ R. Khasanov, T. J. Hicken, D. J. Gawryluk, V. Sazgari, I. Plokhikh, L. P. Sorel *et al.* Pressure-enhanced splitting of density wave transitions in $\text{La}_3\text{Ni}_2\text{O}_{7-\delta}$, *Nat. Phys.* **21**, 430 (2025).

⁴⁸ K. Chen, X. Liu, J. Jiao, M. Zou, C. Jiang, X. Li, *et al.* Evidence of spin density waves in $\text{La}_3\text{Ni}_2\text{O}_{7-\delta}$. *Phys. Rev. Lett.* **132**, 256503 (2024).

⁴⁹ K. Chen, X. Liu, Y. Wang, J. Han, Z. Zhu, J. Jiao, C. Jiang, Y. Guo, C. Zheng, and L. Shu, Effect of Pr-doping and oxygen vacancies on spin density wave in $\text{La}_3\text{Ni}_2\text{O}_{7-\delta}$: A μ SR investigation. *Phys. Rev. Research* **7**, L032014 (2025).

⁵⁰ X.-S. Ni, Y. Ji, L. He, T. Xie, D.-X. Yao, M. Wang, and K. Cao, Spin density wave in the bilayered nickelate $\text{La}_3\text{Ni}_2\text{O}_{7-\delta}$ at ambient pressure. *npj Quantum Mater.* **10**, 17 (2025).

⁵¹ D. Zhao, Y. B. Zhou, M. W. Huo, Y. Wang, L. Nie, Y. Yang, *et al.* Pressure-enhanced spin-density-wave transition in double-layer nickelate $\text{La}_3\text{Ni}_2\text{O}_{7-\delta}$, *Sci. Bull.* **70**, 1239 (2025).

⁵² J. Luo, J. Feng, G. Wang, N. Wang, J. Dou, A. Fang, J. Yang, J. Cheng, G. Zheng, and R. Zhou, Microscopic evidence of charge- and spin-density waves in $\text{La}_3\text{Ni}_2\text{O}_{7-\delta}$ Revealed by ^{139}La -NQR. *Chin. Phys. Lett.* **42**, 067402 (2025).

⁵³ F. Lechermann, J. Gondolf, S. Bötz, and I. M. Eremin, Electronic correlations and superconducting instability in $\text{La}_3\text{Ni}_2\text{O}_7$ under high pressure. *Phys. Rev. B* **108**, L201121 (2023).

⁵⁴ Y. Zhang, L. F. Lin, A. Moreo, T. A. Maier, and E. Dagotto, Trends in electronic structures and *s*-wave pairing for the rare-earth series in bilayer nickelate superconductor $\text{R}_3\text{Ni}_2\text{O}_7$, *Phys. Rev. B* **108**, 165141 (2023).

⁵⁵ Y. Zhang, L. F. Lin, A. Moreo, T. A. Maier, and E. Dagotto, Structural phase transition, *s*-wave pairing and magnetic stripe order in the bilayered nickelate superconductor $\text{La}_3\text{Ni}_2\text{O}_7$ under pressure. *Nat. Commun.* **15**, 2470 (2023).

⁵⁶ H. Oh and Y.-H. Zhang, Type-II $t - J$ model and shared superexchange coupling from Hund's rule in superconducting $\text{La}_3\text{Ni}_2\text{O}_7$, *Phys. Rev. B* **108**, 174511 (2023).

⁵⁷ Z. H. Luo, B. Lv, M. Wang, W. Wu, and D.-X. Yao High- T_c superconductivity in $\text{La}_3\text{Ni}_2\text{O}_7$ based on the bilayer two-orbital $t-J$ model. *npj Quantum Mater.* **9**, 61 (2024).

⁵⁸ H. Sakakibara, N. Kitamine, M. Ochi, and K. Kuroki, Possible high- T_c superconductivity in $\text{La}_3\text{Ni}_2\text{O}_7$ under high pressure through manifestation of a nearly half-filled bilayer Hubbard model. *Phys. Rev. Lett.* **132**, 106002 (2024).

⁵⁹ Y.-B. Liu, J.-W. Mei, F. Ye, W.-Q. Chen, and F. Yang, $s\pm$ -wave pairing and the destructive role of apical-oxygen deficiencies in $\text{La}_3\text{Ni}_2\text{O}_7$ under pressure. *Phys. Rev. Lett.* **131**, 236002 (2023).

⁶⁰ Q. G. Yang, D. Wang, and Q. H. Wang, Possible $s\pm$ -wave superconductivity in $\text{La}_3\text{Ni}_2\text{O}_7$. *Phys. Rev. B* **108**, L140505 (2023).

⁶¹ Y.-H. Tian, Y. Chen, J.-M. Wang, R.-Q. He, and Z.-Y. Lu, Correlation effects and concomitant two-orbital $s\pm$ -wave superconductivity in $\text{La}_3\text{Ni}_2\text{O}_7$ under high pressure. *Phys. Rev. B* **109**, 165154 (2024).

⁶² G. Heier, K. Park, and S. Y. Savrasov, Competing d_{xy} and $s\pm$ -pairing symmetries in superconducting $\text{La}_3\text{Ni}_2\text{O}_7$: LDA+FLEX calculations. *Phys. Rev. B* **109**, 104508 (2024).

⁶³ Y. Gu, C. Le, Z. Yang, X. Wu, and J. Hu, Effective model and pairing tendency in bilayer Ni-based superconductor $\text{La}_3\text{Ni}_2\text{O}_7$. *Phys. Rev. B* **111**, 174506 (2025).

⁶⁴ J.-H. Ji, C. Lu, Z.-Y. Shao, Z. Pan, F. Yang, and C. Wu, A strong-coupling-limit study on the pairing mechanism in the pressurized $\text{La}_3\text{Ni}_2\text{O}_7$. *Phys. Rev. B* **112**, 214515 (2025).

⁶⁵ J.-Y. You, Z. Zhu, M. Ben, W. Chen, and Z. Li. Unlikelihood of a phonon mechanism for the high-temperature superconductivity in $\text{La}_3\text{Ni}_2\text{O}_7$. *npj Comput. Mater.* **11**, 3 (2025).

⁶⁶ J. Zhan, Y. Gu, X. Wu, and J. Hu, Cooperation between electron-phonon coupling and electronic interaction in bilayer nickelates $\text{La}_3\text{Ni}_2\text{O}_7$. *Phys. Rev. Lett.* **134**, 136002 (2025).

⁶⁷ K.-Y. Jiang, Y.-H. Cao, Q.-G. Yang, H.-Y. Lu, and Q.-H. Wang, Theory of pressure dependence of superconductivity in bilayer nickelate $\text{La}_3\text{Ni}_2\text{O}_7$. *Phys. Rev. Lett.* **134**, 076001 (2025).

⁶⁸ Z. Pan, C. Lu, F. Yang, and C. Wu, Effect of rare-earth element substitution in superconducting $\text{R}_3\text{Ni}_2\text{O}_7$ under pressure. *Chin. Phys. Lett.* **41**, 087401 (2024).

⁶⁹ M. Zhang, C. Pei, Q. Wang, Y. Zhao, C. Li, W. Cao, *et al.* Effects of pressure and doping on Ruddlesden-Popper phases $\text{La}_{n+1}\text{Ni}_n\text{O}_{3n+1}$. *J. Mater. Sci. Technol.* **185**, 147 (2024).

⁷⁰ G. Wang, N. Wang, T. Lu, S. Calder, J. Yan, L. Shi, *et al.* Chemical versus physical pressure effects on the structure transition of bilayer nickelates. *npj Quantum Mater.* **10**, 1 (2025).

⁷¹ Z. Huo, Z. Luo, P. Zhang, Ai. Yang, Z. Liu, X. Tao, *et al.* Modulation of the octahedral structure and potential superconductivity of $\text{La}_3\text{Ni}_2\text{O}_7$ through strain engineering. *Sci. China-Phys. Mech. Astron.* **68**, 237411 (2025).

⁷² J. Yang, H. Sun, X. Hu, Y. Xie, T. Miao, H. Luo, *et al.*, Orbital-dependent electron correlation in double-layer nickelate $\text{La}_3\text{Ni}_2\text{O}_7$. *Nat. Commun.* **15**, 4373 (2024).

⁷³ Y. Zhang, L. F. Lin, A. Moreo, and E. Dagotto, Electronic structure, dimer physics, orbital-selective behavior, and magnetic tendencies in the bilayer nickelate superconductor $\text{La}_3\text{Ni}_2\text{O}_7$ under pressure. *Phys. Rev. B* **108**, L180510 (2023).

⁷⁴ Z. Dong, G. Wang, N. Wang, W.-H. Dong, L. Gu, Y. Xu, J. Cheng, Z. Chen, and Y. Wang, Interstitial oxygen order and its competition with superconductivity in $\text{La}_3\text{Ni}_2\text{O}_{7+\delta}$. *Nat. Mater.* **24**, 1927 (2025).

⁷⁵ C.-Q. Chen, W. Qiu, Z. Luo, M. Wang, and D.-X. Yao, Electronic structures and superconductivity in Nd-doped $\text{La}_3\text{Ni}_2\text{O}_7$. *Sci. China-Phys. Mech. Astron.* **69**, 247414 (2026).

⁷⁶ F. Li, N. Guo, Q. Zheng, Y. Shen, S. Wang, Q. Cui, *et al.* Design and synthesis of three-dimensional hybrid Ruddlesden-Popper nickelate single crystals. *Phys. Rev. Mater.* **8**, 053401 (2024).

⁷⁷ F. Li, Z. Xing, D. Peng, J. Dou, N. Guo, L. Ma, *et al.* Bulk superconductivity up to 96 K in pressurized nickelate single crystals. *Nature* (2025). <https://doi.org/10.1038/s41586-025-09954-4>.

⁷⁸ Q. Zhong, J. Chen, Z. Qiu, J. Li, X. Huang, P. Ma, M. Huo, H. Dong, H. Sun, and M. Wang, Evolution of the superconductivity in pressurized $\text{La}_{3-x}\text{Sm}_x\text{Ni}_2\text{O}_7$. *arXiv:* 2510.13342.

⁷⁹ J.-J. Feng, T. Han, J.-P. Song, M.-S. Long, X.-Y. Hou, C.-J. Zhang, *et al.*, Unaltered density-wave transition and pressure-induced signature of superconductivity in Nd-doped $\text{La}_3\text{Ni}_2\text{O}_7$. *Phys. Rev. B* **110**, L100507 (2024).

⁸⁰ Z. Qiu, J. Chen, D. V. Semenok, Q. Zhong, D. Zhou, J. Li, *et al.* Interlayer-coupling-enhanced superconductivity near 100 K in $\text{La}_{3-x}\text{Nd}_x\text{Ni}_2\text{O}_7$. *arXiv:* 2510.12359.

⁸¹ T. Xie, M. Huo, X. Ni, F. Shen, X. Huang, H. Sun, *et al.* Strong interlayer magnetic exchange coupling in $\text{La}_3\text{Ni}_2\text{O}_{7-\delta}$ revealed by inelastic neutron scattering. *Sci. Bull.* **69**, 3221 (2024).

⁸² X. Chen, J. Choi, Z. Jiang, J. Mei, K. Jiang, J. Li, *et al.* Electronic and magnetic excitations in $\text{La}_3\text{Ni}_2\text{O}_7$. *Nat. Commun.* **15**, 9597 (2024).

⁸³ Private communications with Prof. Jun Zhao's group at Fudan University, China.

⁸⁴ Z. Zhang, M. Greenblatt, and J. B. Goodenough. Synthesis, structure, and properties of the layered perovskite $\text{La}_3\text{Ni}_2\text{O}_{7-\delta}$. *J. Solid State Chem.* **108**, 402 (1994).

⁸⁵ See Supplemental Materials for the sample characterization, neutron scattering experiments and linear spin-wave theory calculations.

⁸⁶ L. Yang, Y. Sun, X. Deng, W. Cao, X. Ma, *et al.* Crystalline electric field excitations in the Weyl semimetals RAISi ($\text{R} = \text{Ce, Pr, Nd}$). *Phys. Rev. B* **112**, 054439 (2025).

⁸⁷ R. I. Bewley, R. S. Eccleston, K. A. McEwen, S.M. Hayden, M. T. Dove, S. M. Bennington, J. R. Treadgold, R. L. S. Coleman, MERLIN, a new high count-rate spectrometer at ISIS. *Physica B: Condens. Matter* **385**, 1029 (2006).

⁸⁸ H.-Q. Luo, D. Adroja, H. Zhou, Crystalline Electric Field of Polycrystalline $\text{La}_2\text{NdNi}_2\text{O}_7$, STFC ISIS Neutron and Muon Source, Excitations Xpress Proposal 2590111 (2025). <https://doi.org/10.5286/ISIS.E.RB2590111>

⁸⁹ B. Fåk, S. Rols, G. Manzin, and O. Meulien, Panther—the new thermal neutron time-of-flight spectrometer at the ILL. *EPJ Web of Conferences* **272**, 02001 (2022).

⁹⁰ H. Luo, D. T. Adroja, K. M. Marek, and Z. Lu. (2025). Crystalline Electric Field of Polycrystalline $\text{La}_{3-x}\text{RE}_x\text{Ni}_2\text{O}_7$ ($\text{RE} = \text{Pr, Nd}$). Institut Laue-Langevin (ILL) doi:10.5291/ILL-DATA.4-04-536.

Appendix A. SAMPLE CHARACTERIZATION

The $\text{La}_3\text{Ni}_2\text{O}_{7-\delta}$, $\text{La}_2\text{NdNi}_2\text{O}_{7-\delta}$ and $\text{La}_2\text{PrNi}_2\text{O}_{7-\delta}$ polycrystalline samples were synthesized by the sol-gel method according to previous reports^{26,70,84}. The sample mass for each compound was about 5 grams. The phase purity and crystal structure of the our samples were determined by the powder X-ray diffraction (XRD) collected via an *SmartLab* 9 kW diffractometer under high resolution mode at room temperature. The incident beam was set as Cu K_α radiation ($\lambda = 1.5406 \text{ \AA}$), measurements were ranged from 20° to 100° for 2θ . Structural models are refined with the Rietveld method using the Fullprof software package and the refined results are shown in Fig. S1. The refinement results of crystallographic data are listed in Table S1. Although the weighted profile factor R_{wp} is not so small for all three samples, all peaks can be indexed as the orthorhombic phase (space group *Amam*), while no impurity phases are found within the resolution of our XRD measurements. Clearly, the *c*-axis shrinks in Nd and Pr doped samples, both the out-of-plane (intralayer) Ni-O1-Ni and in-plane (interlayer) Ni-O3-Ni bonding angles decrease for smaller ionic radii of Nd and Pr, where the change of Ni-O bonding lengths is not very clear in doped samples, consistent with the previous reports on rare-earth doped bilayer nickelates⁷⁰.

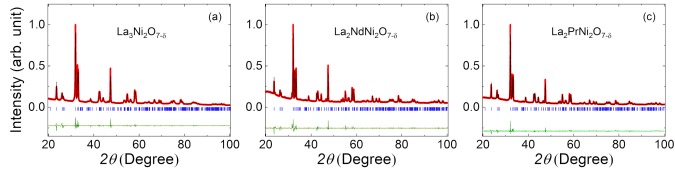


FIG. S1: Powder X-ray diffraction and refinement results of (a) $\text{La}_3\text{Ni}_2\text{O}_{7-\delta}$ (b) $\text{La}_2\text{NdNi}_2\text{O}_{7-\delta}$ (c) $\text{La}_2\text{PrNi}_2\text{O}_{7-\delta}$ samples.

Appendix B. NEUTRON SCATTERING EXPERIMENTS

Inelastic neutron scattering (INS) experiments on $\text{La}_2\text{NdNi}_2\text{O}_{7-\delta}$ were carried out using the MERLIN time-of-flight spectrometer at the ISIS Neutron and Muon Source, Rutherford Appleton Laboratory, UK⁸⁷. The incident energies were selected as $E_i = 15, 24, 50, 79$ and 160 meV^{88} . The INS spectra collected at MERLIN are already shown in Fig. 2 in the main text. Since the $E_i = 160 \text{ meV}$ data could not be found any signals related to the spin excitations but only phonon and incoherent backgrounds, we do not present this data set in our paper.

Further INS measurements were performed at PANTHER time-of-flight spectrometer at the Institut Laue-Langevin, France⁸⁹. The incident energies were selected as $E_i = 19$, and 76 meV for the measurements of $\text{La}_3\text{Ni}_2\text{O}_{7-\delta}$ and $\text{La}_2\text{NdNi}_2\text{O}_{7-\delta}$, and $E_i = 12.5, 19$, and 76 meV for the measurements of $\text{La}_2\text{PrNi}_2\text{O}_{7-\delta}$ ⁹⁰.

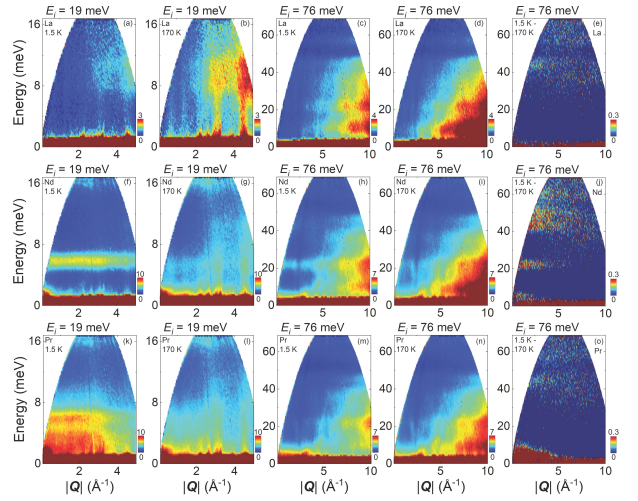


FIG. S2: Raw data of INS spectra of $\text{La}_3\text{Ni}_2\text{O}_{7-\delta}$, $\text{La}_2\text{NdNi}_2\text{O}_{7-\delta}$ and $\text{La}_2\text{PrNi}_2\text{O}_{7-\delta}$ collected at PANTHER with $E_i = 19$ and 76 meV . For comparison, (e),(j) and (o) present the subtracted spectra (1.5 K - 170 K) for all three samples without Bose corrections.

All three samples were measured at the base temperature $T = 1.5 \text{ K}$ and high temperature $T = 170 \text{ K}$. To track the temperature dependence of crystalline electric field (CEF) excitations, we also performed measurements at $T = 50$ and 80 K for $\text{La}_2\text{PrNi}_2\text{O}_{7-\delta}$ sample. Fig. S2 presents the PANTHER data of INS spectra of $\text{La}_3\text{Ni}_2\text{O}_{7-\delta}$, $\text{La}_2\text{NdNi}_2\text{O}_{7-\delta}$ and $\text{La}_2\text{PrNi}_2\text{O}_{7-\delta}$ at $T = 1.5$ and 170 K , along with their differences (Fig. S2 (e),(j) and (o)). It should be noted that we have plotted the intensity as arbitrary unit for convenience, and all subtraction between two temperatures are performed on the same sample, for their same conditions of absorption and self-shielding from the sample and similar background scattering from the empty can. However, since all PANTHER data are normalized by the scattering of an vanadium standard sample, the absolute intensity in the units of $\text{mbarn sr}^{-1} \text{ meV}^{-1} \text{ f.u.}^{-1}$ can be roughly obtained by dividing a factor of 10 from all plots in Fig. 3, Fig. 4, Fig. S2 and Fig. S3, if it requires to compare with other systems. Clear CEF excitations can be observed at 5.5 and 22 meV for $\text{La}_2\text{NdNi}_2\text{O}_{7-\delta}$ (Fig. S2(f) and (h)), while CEF signals in $\text{La}_2\text{PrNi}_2\text{O}_{7-\delta}$ are seen below 8 meV (Fig. S2(k)). Strong phonon signals dominate at the large momentum transfer range. After subtracting the data for high temperature (1.5 K - 170 K), $\text{La}_3\text{Ni}_2\text{O}_{7-\delta}$ shows weak flat-mode spin excitations around 45 meV (Fig. S2(e)), consistent with the results of previous report⁸¹. Splitting spin excitations around 45 meV can be observed both for $\text{La}_2\text{NdNi}_2\text{O}_{7-\delta}$ and $\text{La}_2\text{PrNi}_2\text{O}_{7-\delta}$ (Fig. S2(j) and (o)). Here at such high energy of spin excitations, the correction of Bose population factor $f_B = [1 - \exp(-\hbar\omega/k_B T)]$ is nearly negligible according to the fluctuation-dissipation theorem. Fig. S3 presents the 1D energy cuts at different $|\mathbf{Q}|$ ranges in Fig. S2, where the signals of

TABLE S1: XRD refinement results of crystallographic data for three samples

Parameters	$\text{La}_3\text{Ni}_2\text{O}_{7-\delta}$	$\text{La}_2\text{NdNi}_2\text{O}_{7-\delta}$	$\text{La}_2\text{PrNi}_2\text{O}_{7-\delta}$
Space group	Amam	Amam	Amam
R_{wp}	13.4	16.4	11.2
χ^2	2.33	1.75	1.37
a (Å)	5.400	5.367	5.376
b (Å)	5.451	5.456	5.451
c (Å)	20.500	20.357	20.387
Ni-O1-Ni angle (deg)	168.35	165.49	162.10
Ni-O3-Ni angle (deg)	171.65	166.73	164.64
Ni-O4-Ni angle (deg)	167.76	168.60	166.04
Ni-O1 length (Å)	2.031	1.978	2.030
Ni-O2 length (Å)	2.169	2.198	2.096
Ni-O3 length (Å)	1.903	1.903	1.991
Ni-O4 length (Å)	1.950	1.947	1.871

$\text{La}_2\text{NdNi}_2\text{O}_{7-\delta}$ and $\text{La}_2\text{PrNi}_2\text{O}_{7-\delta}$ are much stronger than those in $\text{La}_3\text{Ni}_2\text{O}_{7-\delta}$. From the difference between 1.5 K and 170 K after correcting by the Bose factor, CEF and spin excitations can be identified by peak features. Indeed, the spin excitation at 45 meV of $\text{La}_3\text{Ni}_2\text{O}_{7-\delta}$ splits into 43, 48 meV and 44, 47 meV in $\text{La}_2\text{NdNi}_2\text{O}_{7-\delta}$ and $\text{La}_2\text{PrNi}_2\text{O}_{7-\delta}$ as shown in the Fig. S3(e) and (h), respectively. To compare the phonon intensities, we also perform the 1D cut with $|\mathbf{Q}| = [6, 10] \text{ \AA}^{-1}$ for $E_i = 76 \text{ meV}$ (Fig. S3(c),(f) and (i)), although the phonon spectra of Nd and Pr doped samples are slightly stronger than the pure La sample, the overall feature and mode energies are the same. It should be noted that the phonon background from the aluminum sample can be included in such high $|\mathbf{Q}|$ range. The phonon background becomes similar at low $|\mathbf{Q}|$ range for all three samples^{65,81}, while electron-phonon coupling alone is insufficient to trigger superconductivity in $\text{La}_3\text{Ni}_2\text{O}_{7-\delta}$ under pressure⁶⁶. Therefore, it is reasonable to search the spin excitations by subtracting the raw data of $\text{La}_3\text{Ni}_2\text{O}_{7-\delta}$ from those results of $\text{La}_2\text{NdNi}_2\text{O}_{7-\delta}$ and $\text{La}_2\text{PrNi}_2\text{O}_{7-\delta}$.

Appendix C. LINEAR SPIN-WAVE THEORY CALCULATIONS

To determine the specific magnitudes of the magnetic exchange couplings, we used the SpinW software package and calculated the dispersion relations of the double spin stripe (DSS), single spin-charge stripe (SCS), A-type antiferromagnetic order (AFM-A), and G-type antiferromagnetic order (AFM-G) based on the Linear Spin-Wave Theory(LSWT).

The basic procedure for calculating the spin dynamical dispersion relations is shown as follows: First, we consider the Hamiltonian by using the Heisenberg model

$$H = \sum_{\langle i,j \rangle} J_{ij} \mathbf{S}_i \cdot \mathbf{S}_j, \quad (2)$$

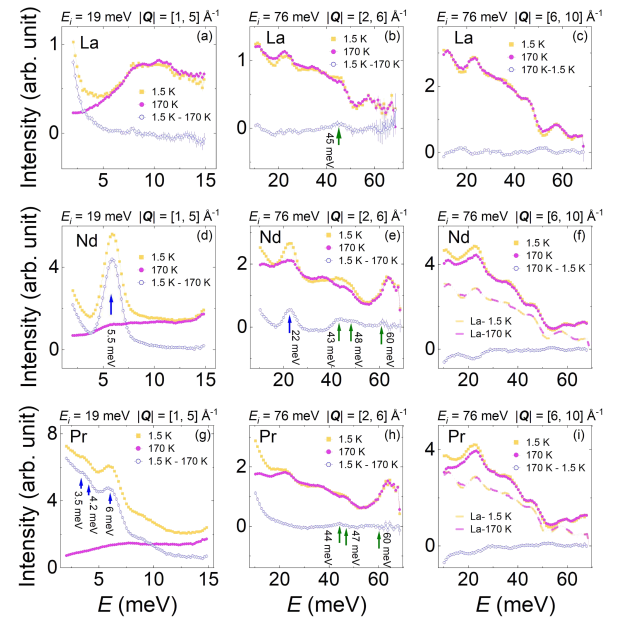


FIG. S3: E -cuts at different regions $|\mathbf{Q}| = [1, 5], [2, 6]$ and $[6, 10] \text{ \AA}^{-1}$ for $\text{La}_3\text{Ni}_2\text{O}_{7-\delta}$, $\text{La}_2\text{NdNi}_2\text{O}_{7-\delta}$ and $\text{La}_2\text{PrNi}_2\text{O}_{7-\delta}$. All data are corrected by the Bose factor to easily compare between different temperatures. The solid symbols represent the original data at $T = 1.5$ and 170 K , and the open symbols are their differences. The blue arrows mark the CEF excitations, and the green arrows mark the spin excitations, respectively. The phonon excitations from the sample and aluminum can dominate at high $|\mathbf{Q}|$ range $[6, 10] \text{ \AA}^{-1}$, where both Nd and Pr doped samples have similar phonon mode energies with pure La sample (dashed lines in (f) and (i)).

where S_i denotes the spin operator on each site i , $\langle i, j \rangle$ denotes neighbor sites. J_{ij} is the exchange interactions between i th and j th spins. Using the commutation relations of angular momentum operators and introducing

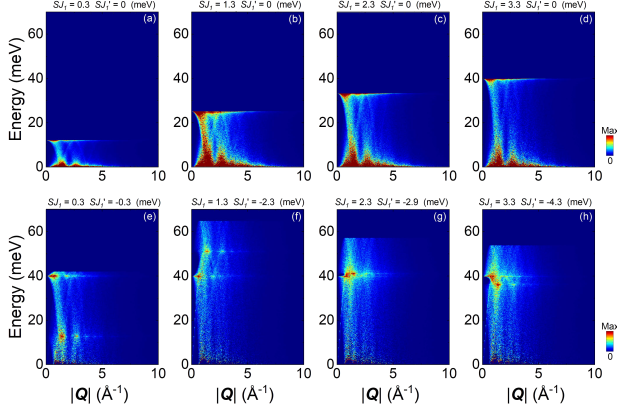


FIG. S4: SpinW calculations based on the double spin stripe (DSS) by fixing $SJ_{\perp} = 60$ meV. (a)-(d) SpinW calculations by only considering the nearest-neighbor intralayer AF exchange coupling J_1 . (e)-(h) SpinW calculations by considering both the nearest-neighbor AF-type intralayer exchange coupling J_1 and the nearest-neighbor FM-type exchange coupling J'_1 .

S^{\pm} , we have

$$H = \sum_{\langle i,j \rangle} J_{ij} [S_i^z \cdot S_j^z + \frac{1}{2} (S_i^+ \cdot S_j^- + S_i^- \cdot S_j^+)], \quad (3)$$

where $S_i^{\pm} = S_i^x \pm S_i^y$. To further diagonalize the Hamiltonian, we perform the Holstein-Primakoff transformation, introduce spin deviation quantum number $n_i = S - m_i$ as well as its corresponding creation and annihilation operators a_i

$$\begin{cases} a_i |n_i\rangle = \sqrt{n_i} |n_i - 1\rangle \\ a_i^\dagger |n_i\rangle = \sqrt{n_i + 1} |n_i + 1\rangle \\ a_i^\dagger a_i |n_i\rangle = \sqrt{n_i} |n_i\rangle \end{cases} \quad (4)$$

and perform a Fourier transform on a_i

$$a_i = N^{-\frac{1}{2}} \sum_k e^{ik \cdot R_i} a_k, a_i^\dagger = N^{-\frac{1}{2}} \sum_k e^{ik \cdot R_i} a_k^\dagger. \quad (5)$$

From this, we can obtain the Hamiltonian under the low-temperature approximation

$$H = E_{Cl} + \sum_{k, \langle i,j \rangle} C_{ii} a_{k,i}^\dagger a_{k,i} + C_{ij} (a_{k,i} a_{k,j} + a_{k,i}^\dagger a_{k,j}^\dagger), \quad (6)$$

where E_{Cl} is the ground state energy. It should be noted that the indices i and j here do not refer to the i th or j th lattice sites in real space, but to the a_k operators corresponding to different lattice sites within a unit cell. If there are a total of i lattice sites in a unit cell, there will be i corresponding a_k operators. C_{ii}, C_{ij} are coefficients related to the specific lattice point in the unit cell. We diagonalize the Hamiltonian using the extended Bogoliubov transformation

$$b_{k,i} = \sum_j m_{ij} a_{k,j} + m'_{ij} a_{k,j}^\dagger. \quad (7)$$

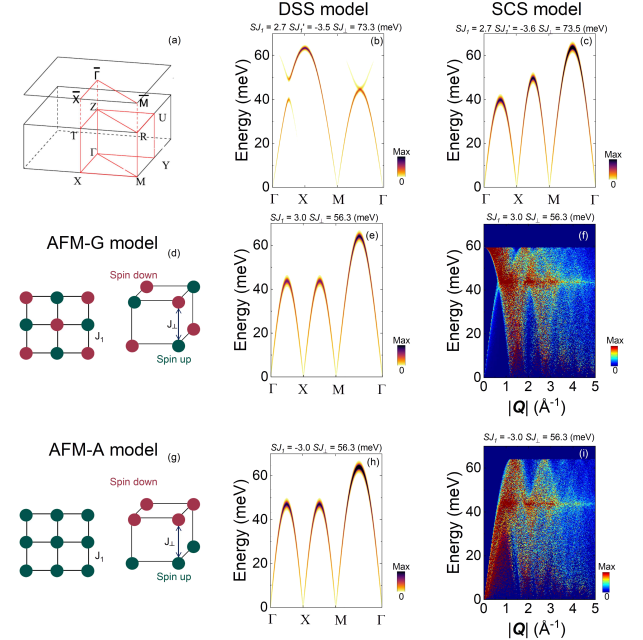


FIG. S5: Spin wave dispersions and magnetic configurations in our SpinW models. (a) Brillouin zone of $\text{La}_3\text{Ni}_2\text{O}_{7-\delta}$. (b) and (c) Spin wave dispersions obtained from fitting parameters of exchange couplings for DSS and SCS models listed in Table. 1 and Fig. 1. (d)-(f) Spin configuration, exchange couplings, dispersion and spectrum for G-type AF model (AFM-G) with $SJ_1 = 3.0$ meV and $SJ_{\perp} = 56.3$ meV. (d)-(f) Spin configuration, exchange couplings, dispersion and spectrum for A-type AF model (AFM-A) with $SJ_1 = -3.0$ meV and $SJ_{\perp} = 56.3$ meV.

By substituting the transformed Hamiltonian into the quantum equation of motion

$$i\hbar \dot{b}_{k,i} = [b_{k,i}, H], \quad (8)$$

the spin dynamical dispersion relations can be obtained accordingly. Considering the simplicity of the model, only the nearest-neighbor interactions were taken into account in our calculations. Therefore, the Hamiltonian expression of the DSS state could be presented as:

$$H = J_1 \sum_{\langle i,j \rangle} S_i \cdot S_j + J'_1 \sum_{\langle i,j \rangle'} S_i \cdot S_j + J_{\perp} \sum_i S_i^t \cdot S_i^b, \quad (9)$$

where J_1 and J'_1 are the antiferromagnetic (AF) and ferromagnetic (FM) intralayer nearest-neighbor interactions, J_{\perp} is the interlayer nearest-neighbor interaction, $\langle i,j \rangle$ and $\langle i,j \rangle'$ denote the intralayer nearest-neighbor lattice sites, and S^t, S^b denotes the spins at the nearest-neighbor lattice site for the top and bottom layers.

By fixing $SJ_{\perp} = 60$ meV and setting $SJ'_1 = 0$, it can be obtained that when SJ_1 varies within the range of $0.3 \sim 3.3$ meV, a distinct flat mode forms in the excitation spectrum of powder sample (Fig.S4 (a)-(d)). Meanwhile, the larger value of SJ_1 , the higher energy of this

mode. This confirms that the prominent flat-band excitation spectrum observed in experiments arises from the interlayer interaction, which is much stronger than the intralayer interaction⁸¹. When FM-type SJ'_1 is further introduced while keeping $SJ_{\perp} = 60$ meV unchanged, adjusting the magnitude of the intralayer nearest-neighbor interaction can account for the splitting excitation spectrum around 45 meV in the rare-earth doped compounds (Fig.S4 (e)-(h)).

Similarly, the Hamiltonian expression of the SCS model is shown as follows:

$$H = J_2 \sum_{\langle i,j \rangle} S_i \cdot S_j + J'_2 \sum_{\langle i,j \rangle'} S_i \cdot S_j + J_{\perp} \sum_i S_i^t \cdot S_i^b. \quad (10)$$

Here, J_2 and J'_2 denote the AF and FM intralayer nearest-neighbor interactions along the diagonal directions in the orthorhombic lattice, respectively. We present the calculated dispersion relations for DSS and SCS models in Fig.S5 (b) and (c). The splitting flat excitations originate either from the band gap in between Γ and X points for DSS model, or from the different band-

tops between the paths of Γ to X and X to M points. Further INS measurements on single-crystalline samples are highly desired to resolve this issue.

In contrast, the Hamiltonians of the AFM-A and AFM-G models can be uniformly expressed as follows:

$$H = J_1 \sum_{\langle i,j \rangle} S_i \cdot S_j + J_{\perp} \sum_i S_i^t \cdot S_i^b, \quad (11)$$

where for AFM-A, J_1 is an antiferromagnetic interaction, and for AFM-G, J_1 is a ferromagnetic interaction. Setting $SJ_1 = 3$ meV and $SJ_{\perp} = 60$ meV, it can be observed that the excitation spectrum exhibits wave-like characteristics rather than flat-band characteristic even for powder sample (Fig.S5 (d)-(i)), which is inconsistent with the experimental results. Furthermore, it cannot explain the splitting observed in $\text{La}_2\text{NdNi}_2\text{O}_{7-\delta}$ and $\text{La}_2\text{PrNi}_2\text{O}_{7-\delta}$, since the bandtops between Γ to X and X to M points are always the same. Therefore, our experimental results can rule out the possibility of AFM-A and AFM-G models in the bilayer nickelate system.